Journal of Magnetic Resonance 352 (2023) 107493

Contents lists available at ScienceDirect

Journal of Magnetic Resonance

journal homepage: www.elsevier.com/locate/jmr

Deuteron off-resonance rotating frame relaxation for the characterization of slow motions in rotating and static solid-state proteins

Liliya Vugmeyster [a,*], Aryana Rodgers [a], Dmitry Ostrovsky [b], C. James McKnight [c], Riqiang Fu [d]

[a] Department of Chemistry, University of Colorado Denver, Denver, CO 80204, USA
[b] Department of Mathematics, University of Colorado Denver, Denver, CO 80204, USA
[c] Department of Pharmacology, Physiology and Biophysics, Boston University Chobanian and Avedisian School of Medicine, Boston, MA 02118, United States
[d] National High Field Magnetic Laboratory, Tallahassee, FL 32310, USA

ARTICLE INFO

Article history:
Received 22 March 2023
Revised 24 May 2023
Accepted 25 May 2023
Available online 30 May 2023

Keywords:
Rotating frame relaxation
Deuterium NMR
Protein dynamics
Off-resonance relaxation

ABSTRACT

We demonstrate the feasibility of deuterium solid-state NMR off-resonance rotating frame relaxation measurements for studies of slow motions in biomolecular solids. The pulse sequence, which includes adiabatic pulses for magnetization alignment, is illustrated for static and magic-angle spinning conditions away from rotary resonances. We apply the measurements for three systems with selective deuterium labels at methyl groups: a) a model compound, Fluorenylmethyloxycarbonyl methionine-D_3 amino acid, for which the principles of the measurements and corresponding motional modeling based on rotameric interconversions are demonstrated; b) amyloid-$\beta_{1\text{-}40}$ fibrils labeled at a single alanine methyl group located in the disordered N-terminal domain. This system has been extensively studied in prior work and here serves as a test of the method for complex biological systems. The essential features of the dynamics consist of large-scale rearrangements of the disordered N-terminal domain and the conformational exchange between the free and bound forms of the domain, the latter one due to transient interactions with the structured core of the fibrils. and c) a 15-residue helical peptide which belongs to the predicted α-helical domain near the N-terminus of apolipoprotein B. The peptide is solvated with triolein and incorporates a selectively labeled leucine methyl groups. The method permits model refinement, indicating rotameric interconversions with a distribution of rate constants.

1. Introduction

Internal motions in proteins on the μs-ms time scale are essential for functioning of proteins, nucleic acids and complex biological systems [1–3]. Relaxation dispersion approaches for proteins in the solid state have been recently developed and described in detail [2,4–15], with major efforts devoted to ^{15}N, ^{13}C, and ^{1}H nuclei [10,14,16,17]. Rotating frame relaxation ($R_{1\rho}$) experiments in solids have the capacity to probe both the fluctuations of the isotropic chemical shift component and the fluctuations of the anisotropic tensor due to conformational changes [14]. Under magic angle spinning (MAS) conditions, the latter has been shown to modulate the width of rotational resonances [12,13].

Deuterium is spin-1 nucleus with the typical quadrupolar coupling constant (C_q) in 150 to 200 kHz range [18–20]. Deuterium NMR relaxation has proven to be a sensitive tool for measuring the dynamics in a variety of systems [18,19,21–23]. The relaxation is governed primarily by the quadrupole interaction [18]. We previously developed the on-resonance $R_{1\rho}$ experiment for ^{2}H nuclei under static conditions [24] and rotating solids [15].

The goal of this work is to show the development and applications of the off-resonance ^{2}H $R_{1\rho}^{off}$ experiment for proteins in the solid-state under magic-angle spinning (MAS) and static conditions. Recent literature emphasizes the extension of conventional deuterium NMR approaches for multiply-labeled systems under MAS conditions [25–29]. The off-resonance condition has been extensively exploited in solution and solid state NMR applications, as it allows for application of larger spin-locking fields without the additional RF-induced heating [3,30]. Larger spin-locking fields provide an advantage of extending the window of time scale of the motional modes probed by the measurements, Inn certain cases it also permits for more accurate determination of motional parameters, as well as for the refinement of the motional models.

* Corresponding author at: Department of Chemistry, University of Colorado at Denver, 1201 Larimer St, Denver, CO 80204.
E-mail address: LILIYA.VUGMEYSTER@UCDENVER.EDU (L. Vugmeyster).

https://doi.org/10.1016/j.jmr.2023.107493
1090-7807/

We demonstrate the applicability of the $R_{1\rho}^{off}$ deuterium NMR relaxation experiments under MAS and static conditions for three systems with selective deuterium labels at methyl groups: A) a model compound Fluorenylmethyloxycarbonyl (FMOC) methionine-D_3 amino acid, for which we demonstrate the principles of the measurements. The μs-ms time scale motions of the methionine side-chains are dominated by large-angle rotameric jumps (Fig. 1A). B) amyloid-$\beta_{1\text{-}40}$ fibrils labeled at a single alanine methyl group located in the disordered N-terminal domain [31]. We previously determined the details of the dynamics for this system with other deuterium solid-state NMR measurements, such as on-resonance ^2H $R_{1\rho}$ and Quadrupolar Chemical Exchange Saturation Transfer (Q-CEST), and Quadrupolar Carr-Purcell-Meiboom-Gill (Q-CPMG) experiments.[15,31,32] The measurements on the hydrated fibrils comprised of the amyloid-$\beta_{1\text{-}40}$ protein [33] in the three-fold symmetric polymorph [33,34] serve as a confirmation of the method for complex biological systems, as the disordered domain undergoes conformational exchange between the free state and the bound state that transiently interacts with the fibrils' core (Fig. 1B). C) A 15-residue, highly hydrophobic, helix-6 (H6) with a selectively labeled leucine methyl group, which is part of the predicted α-helical domain of apolipoprotein B (apoB) (Fig. 1C) [35,36]. ApoB the essential protein component of triacylglycerol rich lipoproteins including chylomicrons and very low density lipoprotein (VLDL) and also low density lipoprotein (LDL, "the bad cholesterol"). The α-helical domain was shown to be spontaneously adsorbed to a triolein/water interface and formed a viscoelastic surface [36]. It was anchored irreversibly to the surface by H6. In our studies we thus solvate the H6 construct with triolein to mimic its native environment. The new measurements

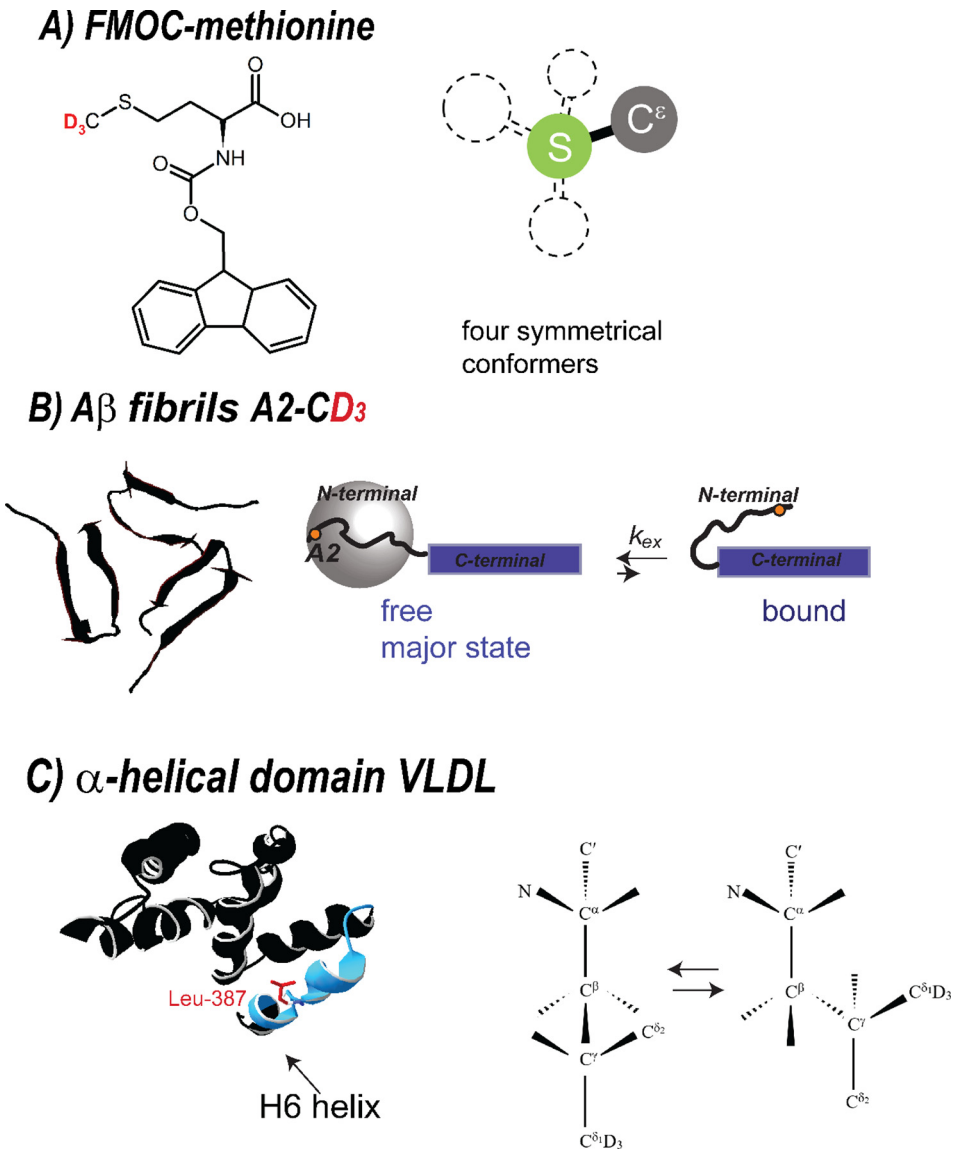

Fig. 1. A) Left: structure of FMOC-methionine amino acid with the deuterated methyl group highlighted in red. Right: the model of inter-conversions between four artificial conformers with the tetrahedral geometry, in lieu of the exact model of 27 rotamers in the methionine side-chain.[37] B) Left: the 3-fold symmetric fibrils structure, top view. [34] Right: schematic representation of the two-site exchange model, in which the disordered N-terminal domain (curved line) transiently interacts with the structured C-terminal domain (blue rectangle). In the free state, the N-terminal domain is assumed to undergo isotropic diffusion, as represented by the gray sphere, while in the bound state, transient interactions with the hydrophobic core quench this mode.[31] The position of the labeled methyl group in the A2 residue is shown as an orange dot. C) Left: the α-helical domain of VLDL [35,36]. The location of the 15-residue H6 helix is shown with the arrow and the corresponding ribbon diagram is colored in light blue. The Leu-387 side chain, which has deuterated methyl groups, is shown in red. Right: the two-site rotameric exchange model of methyl axis in the leucine side-chain, displaying two most likely rotamers. (For interpretation of the references to colour in this figure legend, the reader is referred to the web version of this article.)

permit the model refinement of the rotameric jumps of the labeled leucine side-chain.

2. Experimental

2.1. Materials

FMOC-methionine-CD_3 was purchased from CDN isotopes (Pointe-Claire, Canada). The monomeric sequence of the $A\beta_{1\text{-}40}$ peptide is D[A − CD_3]EFRHDSGYEVHHQKLVFFAEDVGSNKGAIIGLMVGGVV. The $A\beta_{1\text{-}40}$ fibrils, labeled at the A2-CD_3 site, were prepared as previously described in the 3-fold symmetric polymorph [31,38] and packed into a 5 mm glass tube for static measurement. The fibrils were hydrated to 200% by weight with deuterium-depleted water using direct pipetting and equilibrating at room temperature for 5 days.

The H6 peptide with the sequence PLLIDVVTY[L-CD_3]VALIP (residues 378–391 of human apoB) was prepared using solid-state peptide synthesis. FMOC-Leucine-5,5,5-D_3 was purchased from Cambridge Isotope Laboratories. The peptide was solvated to 50% by weight with triolein and packed into a 1.3 mm rotor.

All synthetic peptides were prepared and purified by Thermofisher Scientific, Inc. The identity and purity of the peptides was confirmed by matrix-assisted laser desorption/ionization mass spectroscopy mass spectroscopy and reversed-phase analytical HPLC at 95–98% purity level (C18 column, 0.5% acetonitrile/min gradient).

2.2. NMR spectroscopy

Static $R_{1\rho}^{off}$ measurements were conducted using the 400 MHz spectrometer at CU Denver equipped with a Phoenix static probe with a 5 mm coil. For FMOC-methionine the spin-locking field of 30 kHz was employed and the values of offsets ranged from 5 to 105 kHz. The RF field was calibrated using the nutation measurements (Figure S1). Relaxation delays ranged from 0.7 to 28 ms. These values include the adiabatic ramp durations of 0.4 ms. An interscan delay of 2.5 s, 32 scans, and 8 dummy scans were employed. The *tanh*/tan adiabatic pulses described in the "Results and Discussion" section were employed, with the sweep width of 120 kHz. The 90° high power pulse as well as the 180° inversion pulse utilized 125 kHz RF field strength. The Bruker pulse sequence code and the Matlab code for generation of the adiabatic shape pulse are available in SI1 and SI2. For the Aβ fibrils, the spin-lock field was set to 15 kHz, with the range of offsets between 3 and 45 kHz. The *tanh*/tan adiabatic ramp was employed with the sweep of 60 kHz. The magnetization decay curve was sampled between 0.5 and 15 ms. The interscan delay of 1.8 s and 1024 scans were used, with 32 dummy scans. All line shapes were measured using the quadrupolar echo (QE) pulse sequence [18] with the echo delay of 31–35 μs. ^{2}H longitudinal relaxation times (T_1) were measured using the inversion recovery scheme with the QE detection, and were also confirmed with the saturation recovery scheme for FMOC-methionine. Seven to nine relaxation delays were collected with values ranging from 100 μs to 6 × T_1. Spectra were processed with the 1 kHz exponential line broadening function. Magnetization relaxation decay curves $M(t)$ were fitted to a mono-exponential function with a baseline of the form

$$M(t) = Ae^{-R_{1\rho}t} + B \quad (1)$$

The $R_{1\rho}^{off}$ measurements under MAS conditions were conducted using the 600 MHz spectrometer equipped with a 1.3 mm triple resonance probe at the National High Magnetic Field Laboratory. For FMOC-methionine the spin-lock fields, adiabatic ramp parameters, offset ranges, relaxation delays ranges were the same as used in the static case. 10 kHz MAS rate was employed as a major condition, unless otherwise noted in the text. 16 scans were used for FMOC-methionine, while 64 scans were used for the H6 peptide. The sweep width of the adiabatic ramp alignment pulse was 120 kHz in all cases, and the spin-locking field of 30 kHz was used for FMOC-methionine, while two values of the spin-locking fields, 17 and 30 kHz, were used for the H6 peptide. The inter-scan delay was 1.8 s and 2.4 s for 17 and 30 kHz rf fields, respectively. Spectra were processed with the 50 Hz line broadening function and the sum of all side-bands intensities was used to obtain relaxation decay curves.

2.3. Modeling of motions

The rotameric interconversion mode for FMOC-methionine was modeled by four artificial symmetrical conformers with the tetrahedral geometry [37], while for the Leu-387 site of the H6 peptide it was sufficient to include two conformers with the jump angle of 109.5°. The explicit modeling of restricted diffusion along the arc was included for Leu-387 as an additional motional frame with nine sites separated by 5°, as described in [39].

The spherical diffusion motion of the free state of N-terminal domain of Aβ fibrils coupled to the conformational exchange with the bound state was modelled in accordance with procedure outlined in [31]. Spherical diffusion was represented by small-angle jumps between 192 discreet sites with the orientations uniformly distributed on a unit sphere [40], while the bound state was represented by a single additional site with a fixed orientation and in exchange with all free-state sites.

The inclusion of coherent interactions, evolution under MAS, and the details of the detection schemes closely mirrored the procedure described in references [15,24]. In particular, the time dependence under MAS of the Liouvilian matrix was modeled by 20 points equally spaced over a single MAS rotation period.

3. Results and Discussion

3.1. Experimental approach

The off-resonance $R_{1\rho}^{off}$ experiment (Fig. 2) relies on the alignment of magnetization along the effective field, given by the vector sum of ω_{RF}(spin-lock field) and Ω (off-resonance offset), which we will refer to as the tilted axis. As will be elaborated in detail in the *Theory and Computational Approaches* section, the relaxation rate thus has contributions originating from the longitudinal laboratory frame component (T_1), which has to be measured independently or taken into account experimentally. The experiment can also be more precise if one starts with the inversion of the magnetization, in analogy to the inversion recovery experiment. Thus, our pulse sequence consists of the heat compensation block, followed by an optional inversion pulse, followed by the variable-time spin-lock flanked by the alignment elements, the latter described in detail below. The detection block is either a single 90° pulse when the measurement is performed under MAS condition, or can be replaced by the quadrupolar echo detection scheme for the static conditions [18,24]. The experiment is repeated for a series of Ω values and can employ several values of ω_{RF}.

Molecular motions can significantly narrow the line shapes and an efficient alignment of magnetization for deuterium requires optimization of adiabatic shape pulses for specific magnitudes of the effective quadrupolar tensor. Fast methyl rotations average the quadrupolar coupling constant, C_q, by a factor of 1/3 to about 55 kHz, with the possibility of the additional motions further affecting the line shapes [25,28,29]. In our systems additional slow

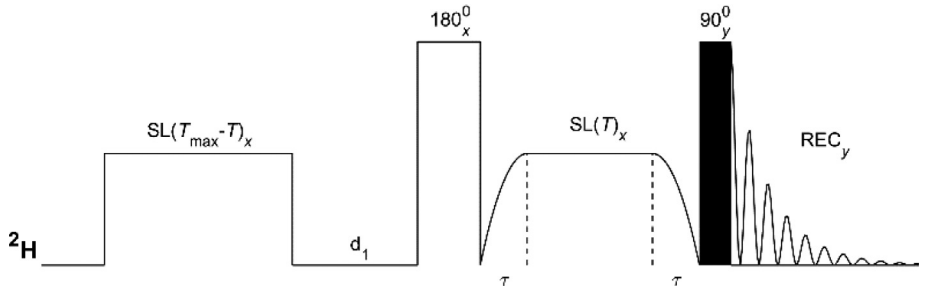

Fig. 2. Pulse sequence for the ^{2}H solid-state static $R_{1\rho}^{off}$ measurements under MAS conditions. The heat compensation block (T_{max}-T) is followed by the inter-scan delay d_1 and the (optional) inversion pulse, followed by a shaped pulse consisting of a variable spin-lock period(T) which is flanked on both sides by the adiabatic alignment ramp of the form *tanh*/tan (Eq.2). The optimized adiabatic shape parameters are α = 1.5, β = 5, τ = 200 μs and the steepness $\Delta\Omega_0$ of 40–120 kHz range. The last 90° pulse immediately precedes FID collection. For the experiment under static condition, the quadrupolar echo detection scheme can be added.

motions lead to the effective magnitudes of the tensor in the 3 to 58 kHz range.

To achieve the adiabatic alignment of the magnetization, we have employed the conventional "*tanh*/tan" shape [30] with the RF field modulations given by

$$\omega_{RF}(t) = \omega_{RF}\frac{\tanh\alpha(t/\tau)}{\tanh\alpha} \tag{2a}$$

where τ is the duration of the ramp and α is the steepness parameter.

The modulation of the offset during the ramp time is given by $\Omega + \Delta\Omega(t)$, where Ω is the final frequency offset after the ramp and $\Delta\Omega(t)$ is the additional offset during the ramp time:

$$\Delta\Omega(t) = \Delta\Omega_0\frac{\tan((\text{atan}\beta)[1-t/\tau])}{\beta} \tag{2b}$$

where $\Delta\Omega_0$ is the sweep and β is the steepness parameter for the offset.

The parameters that require optimization are the steepness α and β, the pulse duration τ, and the sweep $\Delta\Omega_0$. The optimal sweep depends on the effective tensor magnitude [25,41,42], ranging in our cases from 120 kHz for the effective C_q value of 55–58 kHz to 40 kHz for the effective C_q value of 3–10 kHz. A short duration of around 200 μs ensures no significant relaxation occurs during the ramp period. For the short pulse duration of 200 μs the best value of α is around 1.5 with β = 5, as tested computationally for C_q of 55 kHz. Several examples of these optimizations are shown in Fig. 3 and Figure S2. The second ramp brings magnetization along the *z*-axis of the lab frame.

Another obvious option is to perform the alignment with a single hard pulse corresponding to the desired value of the offset. This method is more prone to errors due to pulse calibrations, uneven powder pattern excitation, differences in chemical shifts when multiple conformers or sites are considered, and effects of the RF field inhomogeneity.

If the measurement is performed under MAS, it is important to be aware of multiple rotary resonances at the conditions given by $\omega_{eff} = \frac{n}{2}\omega_{MAS}$, where n is an integer, ω_{MAS} is the MAS rate and ω_{eff} is the effective spin-locking field along the tilted axis. The rotary resonance effect can be included in the analysis but renders the dispersion curve complicated. In this work we thus constrict the off-resonance measurements under MAS to a low spin rate of 10 kHz and RF amplitudes of at least 30 kHz.

3.2. Theory and computational approaches

I. General Equations for $R_{1\rho}^{off}$ relaxation

The basis of the following operators constitutes the density matrix for the spin 1 system:

$$\hat{S}_x = \frac{1}{2}\begin{pmatrix}0&1&0\\1&0&1\\0&1&0\end{pmatrix}, \hat{S}_y = \frac{1}{2}\begin{pmatrix}0&-i&0\\i&0&-i\\0&i&0\end{pmatrix},$$
$$\hat{J}_x = \frac{1}{2}\begin{pmatrix}0&-i&0\\i&0&i\\0&-i&0\end{pmatrix}, \hat{J}_y = \frac{1}{2}\begin{pmatrix}0&1&0\\1&0&-1\\0&-1&0\end{pmatrix} \tag{3}$$
$$\hat{J}_z = \frac{1}{\sqrt{2}}\begin{pmatrix}0&0&-i\\0&0&0\\i&0&0\end{pmatrix}, \hat{K} = \frac{1}{\sqrt{2}}\begin{pmatrix}0&0&1\\0&0&0\\1&0&0\end{pmatrix},$$
$$\hat{S}_z = \frac{1}{\sqrt{2}}\begin{pmatrix}1&0&0\\0&0&0\\0&0&-1\end{pmatrix}, \hat{Q} = \frac{1}{\sqrt{6}}\begin{pmatrix}1&0&0\\0&-2&0\\0&0&1\end{pmatrix}$$

The first row represents the single-quantum coherences, followed by two double-quantum coherences, $\hat{K}$ and $\hat{J}_z.\hat{S}_z$ and $\hat{Q}$ stand for the Zeeman and quadrupolar order. They obey the following normalization condition $tr(O_k^+ O_l) = \delta_{kl}$.

During the spin-locking or saturation periods and in the frame rotating with the Larmor frequency, the secular part of the Hamiltonian is given by

$$\hat{H} = \sqrt{\frac{2}{3}}\omega_Q\hat{Q} + \sqrt{2}\omega_{RF}\left(\hat{S}_x\cos\Omega t - \hat{S}_y\sin\Omega t\right)$$

where ω_{RF} is the spin-l RF field strength and Ω is its off-resonance offset.

$$\omega_Q = \frac{3\pi}{2}C_q\left(\frac{3\cos^2\Theta-1}{2} + \frac{\eta}{2}\sin^2\Theta\cos 2\phi\right) \tag{4}$$

is the frequency of the secular part of quadrupole interaction with the angles (Θ, ϕ) representing the rotation of the principal-axis system (PAS) of the quadrupole interaction with respect to the laboratory frame. The quadrupolar coupling constant is given by $C_q = \frac{e^2qQ}{h}$, and $\eta = \frac{q_{xx}-q_{yy}}{q_{zz}}$ represents the asymmetry of the tensor, defined in the interval $0 \leqslant \eta \leqslant 1$ with $|q_{zz}| \geqslant |q_{yy}| \geqslant |q_{xx}|$. eQ is the electric quadrupole moment of the nucleus and eq is the largest component of the electric field gradient.

Under the MAS conditions and for $\eta = 0$

$$\omega_Q(t) = \frac{3\pi}{4}C_q\Big(\sqrt{2}\sin 2\Theta_{MAS}\sin(\omega_{MAS}t + \phi_{MAS}) - \sin^2\Theta_{MAS}\cos(2\omega_{MAS}t + 2\phi_{MAS})\Big) \tag{5}$$

where Θ_{MAS} and ϕ_{MAS} are the polar and azimuthal angles with respect to the axis of rotation, respectively.

In the frame additionally rotating around the *z*-axis with the offset frequency of Ω, the secular part of the Hamiltonian becomes

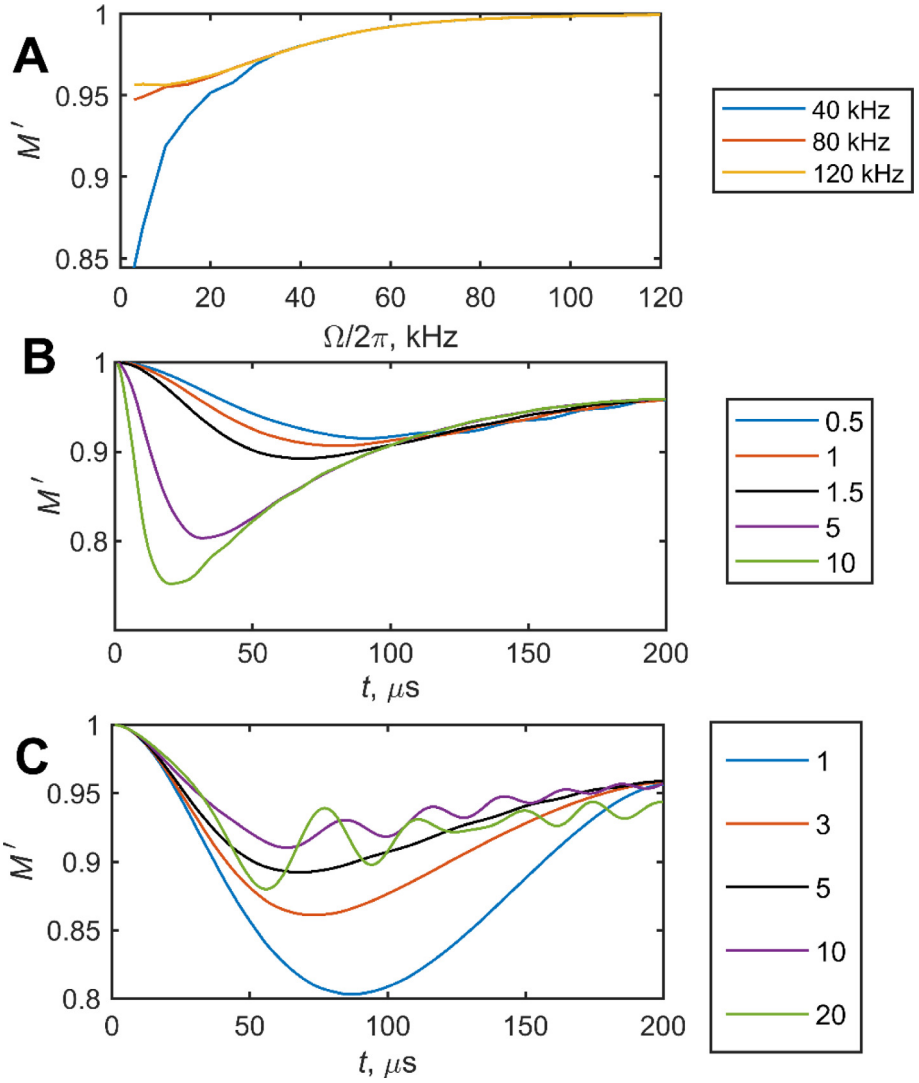

Fig. 3. The effectiveness of the adiabatic magnetization alignment for the *tanh*/tan ramp (Eq. 2) for various parameters. The calculations were performed using C_q = 55 kHz and the spin-lock field of 30 kHz. A) The final magnetization along the tilted axis at the end of the ramp M' as a function of offset Ω for three values of $\Delta\Omega_0$ indicated in the legend, with α = 1.5, β = 5. B) M' along the instantaneous tilted axis during the pulse duration time t for several values of α and β = 5. C) M' along the instantaneous tilted axis during the pulse duration time t for several values of β and α = 1.5. Static conditions were assumed.

$$\widehat{H}_{sec} = \sqrt{\frac{2}{3}}\omega_Q \widehat{Q} + \sqrt{2}\omega_{RF}\widehat{S}_x + \sqrt{2}\Omega\widehat{S}_z \tag{6}$$

The evolution of the density matrix can be written using the basis of Eq.(3) in the superoperator formalism. The matrix defining the evolution equation in Liouville – von Neumann formalism is a sum of the Hamiltonian super-operator for the spin density matrix and Markovian transition rate matrix between states with different values of ω_Q, representing different spin environments. As a result, it implicitly includes the relaxation due to the fluctuations in the ω_Q value, which, in general, cannot be treated within the Redfield approximation. The rapidly oscillating non-secular part of the Hamiltonian is treated in the 2nd order of the perturbation theory, i.e. in the Redfield approximation for rapidly oscillating terms [43]. As we will discuss in detail later, they include all the terms of the spectral density function of the order of the Larmor and twice the Larmor frequency.

If the molecular motions are given by discrete jumps between n sites with different values of ω_Q sampled by the conformational exchange, the evolution matrix becomes

$$\frac{d}{dt}\begin{pmatrix}\rho_1\\ \rho_2\\ \vdots\\ \rho_n\end{pmatrix} = \begin{pmatrix} iL_1 + K_{11} - R_{L,1} & K_{12} & \cdots & K_{1n} \\ K_{21} & iL_2 + K_{22} - R_{L,2} & \cdots & K_{2n} \\ \vdots & \vdots & \ddots & \vdots \\ K_{n1} & K_{n2} & \cdots & iL_n + K_{nn} - R_{L,n} \end{pmatrix} \times \begin{pmatrix}\rho_1\\ \rho_2\\ \vdots\\ \rho_n\end{pmatrix} \tag{7}$$

where $\rho_i = (S_x, S_y, J_x, J_y, J_z, K, S_z, Q)^T$ are the components of the density matrix for the site i in the basis of the operators of Eq.(3). The off-diagonal blocks represent conformational exchange and are given by $K_{ij} = k_{ij}I$, where I is the 8 × 8 identity matrix and the diagonal blocks $K_{ii} = -\sum_{j\neq i} K_{ji}$ provide conservation of probability. The 8 × 8 evolution matrices L_i represent superoperators of the secular part of the Hamiltonian $\widehat{H}_{sec}$ in the basis of ρ_i and are given by:

$$iL = \begin{pmatrix} 0 & -\Omega & -\omega_Q & 0 & 0 & 0 & 0 & 0 \\ \Omega & 0 & 0 & \omega_Q & 0 & 0 & -\omega_{RF} & 0 \\ \omega_Q & 0 & 0 & \Omega & 0 & -\omega_{RF} & 0 & -\sqrt{3}\omega_{RF} \\ 0 & -\omega_Q & -\Omega & 0 & \omega_{RF} & 0 & 0 & 0 \\ 0 & 0 & 0 & -\omega_{RF} & 0 & \Omega & 0 & 0 \\ 0 & 0 & \omega_{RF} & 0 & -\Omega & 0 & 0 & 0 \\ 0 & \omega_{RF} & 0 & 0 & 0 & 0 & 0 & 0 \\ 0 & 0 & \sqrt{3}\omega_{RF} & 0 & 0 & 0 & 0 & 0 \end{pmatrix} \tag{8}$$

The rapidly oscillating terms of the quadrupole interaction contribute to the relaxation of the coherences ρ_i. They can be treated in the Redfield approximation and result in the diagonal relaxation matrix $R_L = \frac{3\pi^2}{2} C_q^2 diag(r_1, r_1, r_2, r_2, r_3, r_3, r_4, r_5)$, with the following terms:[44]

$$\begin{aligned} r_1 &= \tfrac{5}{2} J_1(\omega_L) + J_2(2\omega_L) \\ r_2 &= \tfrac{1}{2} J_1(\omega_L) + J_2(2\omega_L) \\ r_3 &= J_1(\omega_L) + J_2(2\omega_L) \\ r_4 &= J_1(\omega_L) + 4J_2(2\omega_L) \\ r_5 &= 3J_1(\omega_L) \end{aligned} \tag{9}$$

Note that relaxation terms in reference [44] include also relaxation due to changes in ω_Q values, which in this work are calculated in the Liouville – von Neumann formalism and are thus excluded from the R_L. terms of Eq. (9). The J_1 and J_2 terms are treated within the Redfield approximation, based on the assumption that the relaxation rate is significantly smaller than the rate of motions which cause it [43].

II. Relaxation in Redfield limit for static case

All computations done for the comparison with experiment were performed in Liouville – von Neumann framework outlined above. It is, however, instructive to gain some semi-quantitative understanding of the relaxation by adopting a simplifying Redfield approach, which allows for analytical treatment. In the Redfield approximation, a single coherence represents all exchanging sites. Its evolution is governed by the Hamiltonian given in Eq.(6) with the quadrupolar coupling ω_Q averaged over the exchanging sites. The relaxation matrix R_L now includes contributions from the fluctuations of the dipolar coupling calculated in the second order of perturbation theory. Because equilibrium coherence for the Hamiltonian in the absence of excitation is not zero but S_z, the relaxation matrix should multiply $\rho - S_z$ rather than ρ. As the result, the evolution of the coherence vector in the frame rotating around the z-axis with the offset frequency of Ω is given by:

$$\frac{d\rho}{dt} = iL\rho - R(\rho - S_z) \tag{10}$$

where R is the matrix of relaxation rates, which is, in general, non-diagonal.

First, we determine the equilibrium coherence. Assuming that the relaxation rates R are much smaller than oscillation terms iL, we consider the equilibrium coherence in the form $\rho^{eq} = b\rho_0 + \delta\rho$, where ρ_0 is a unitary coherence satisfying $L\rho_0 = 0$ and $tr(\rho_0^+\rho_0) = 1$ and $\delta\rho$ satisfies the condition $tr(\rho_0^+\delta\rho) = 0$. We assume that the $\delta\rho$ term is small, as the relaxation matrix elements in R are much smaller than the oscillatory terms in L under spin-locking conditions. The coefficient b thus serves as the amplitude of the coherence at $t \to \infty$. From the observational point of view, it is therefore seen as baseline of the magnetization decay.

Substitution into Eq. (10) yields

$$\begin{aligned} \frac{d\rho^{eq}}{dt} &= 0 = iL(b\rho_0 + \delta\rho) - R(b\rho_0 + \delta\rho - S_z) \\ &= iL\delta\rho - bR\rho_0 + RS_z - R\delta\rho \end{aligned}$$

Taking trace with the ρ_0 coherence one finds $i \cdot tr(\rho_0^+ L\delta\rho) - tr(\rho_0^+ R\rho_0)b + tr(\rho_0^+ RS_z) - tr(\rho_0^+ R\delta\rho) = 0$. In the first term, $\rho_0^+ L = (L\rho_0)^+ = 0$ because L is a Hermitian operator and the fourth term is of the second order in the relaxation rates. Taking to account only the terms of the first order in R, one can solve for b

$$b = \frac{tr(\rho_0^+ RS_z)}{tr(\rho_0^+ R\rho_0)} \tag{11}$$

To estimate the relaxation rate, we note that the oscillating coherences are rapidly averaged and that the observable coherence is proportional to ρ_0. Thus, the relaxation rate is given by

$$R_{1\rho}^{off} = tr(\rho_0^+ R\rho_0) \tag{12}$$

The Liouville operator iL, given in Eq. (8) has two linearly independent eigenvectors with the eigenvalue zero. Without further approximations, the analytical expressions for the coherence ρ_0 span complicated combinations from all base coherences, which makes analytic calculations cumbersome.

We therefore consider the limit of $\omega_Q \ll \omega_{eff}$, in which case one of the coherences with eigenvalue 0 corresponds to the magnetization along the tilted axis $\rho_0 = (\sin\theta, 0, 0, 0, 0, 0, \cos\theta, 0)$ with $\theta = \tan^{-1}\frac{\Omega}{\omega_{RF}}$. Another coherence with eigenvalue 0, corresponds to the magnetization perpendicular to the tilted axis and can be ignored. The relaxation rate becomes:[45]

$$\begin{aligned} R_{1\rho}^{off} &= tr(\rho_0^+ R\rho_0) \\ &= \frac{3\pi^2}{2} C_q^2 \left[\frac{3}{2} \sin^2\theta \left(\sin^2\theta J_0(2\omega_{eff}) + \cos^2\theta J_0(\omega_{eff}) \right) \right. \\ &\quad \left. + \left(\frac{5}{2} - \frac{3}{2}\cos^2\theta \right) J_1(\omega_L) + (1 + 3\cos^2\theta) J_2(2\omega_L) \right] \end{aligned} \tag{13}$$

The baseline is:

$$b = \frac{tr(\rho_0^+ RS_z)}{tr(\rho_0^+ R\rho_0)} = \frac{\cos\theta R_{1z}}{R_{1\rho}^{off}} \tag{14}$$

where

$$R_1 = \frac{3\pi^2}{2} C_q^2 (J_1(\omega_L) + 4J_2(2\omega_L)) \tag{15}$$

is the usual rate of the longitudinal relaxation. The latter expression follows from the fact that quadrupolar operator $\hat{Q}$ commutes with the operator $\hat{S}_z$ and therefore its fluctuations do not modify the relaxation of S_z coherence. We note that, similar to the case of homonuclear dipolar relaxation of spin-1/2 nuclei [14], $R_{1\rho}^{off}$ is not a simple combination of $R_{1\rho}$ and R_1 due to the structure of the space of coherences of Eq. (3).

Note that in our case the $R_{1\rho}$ term includes all effects due to motions including the "intrinsic relaxation" for terms containing $J(\omega_L)$, which could be viewed as an equivalent of R_2^0 contributions [46]. Additional possible R_2^0 contributions due to dipolar (with external spin I, which would be especially important for the case of a directly bonded ^{13}C nucleus) and ^{2}H CSA interactions are not included in these expressions. The dipolar contributions could be significant for larger values of Ω for which the initial coherence would contain S_zI_z terms.

The spectral density functions J_0, J_1, and J_2 depend on the orientation of a crystallite in the lab frame. For a polycrystalline sample, the observed value of the relaxation rate is derived from the single

exponential fit of the relaxation decay curve [2]. This curve in turn is the average of the relaxation decay curves for the individual crystallites. When the initial coherence can be approximated as the coherence of norm 1 aligned along the tilted axis, $\rho_0 = (\sin\theta, 0, 0, 0, 0, 0, \cos\theta, 0)$, the relaxation leads to magnetization decay between the values of 1 and b of Eqs. (13)–(15), corresponding to the amplitude change of $1 - b$.

On the contrary, when the initial coherence is $-\rho_0$, as is the case for the relaxation experiment with inversion, the amplitude changes between the values of -1 and b, corresponding to the overall change in amplitude of $1 + b$. We will demonstrate that for a large class of applications relevant to the study of the side-chain dynamics of proteins, the dependence of $R_{1\rho}^{off}$ on crystalline orientation is much more pronounced than the dependence of the R_1 term. If this is the case, the larger value of $R_{1\rho}^{off}$ is positively correlated with the smaller value of the baseline b and, therefore, with the larger value of the amplitude change in the magnetization in the experiment without initial inversion. The larger change of the magnetization amplitude for a particular crystallite orientation leads to the larger weight given to the relaxation rate associated with this orientation in the averaging procedure based on the averaging of the relaxation curves over all orientations. Thus, the initial condition with no inversion renders the overall observed relaxation rate larger, due to the orientation-dependent baseline effect. Conversely, when the initial magnetization is produced with inversion, the baseline effect will lead to a smaller relaxation rate. This is elaborated in more detail in SI3.

To demonstrate this difference in orientation dependencies, we have performed a simple simulation (Fig. 4) with the model similar to what we will encounter for some of the experimental cases in the following section. The model includes the fast methyl three-site jump mode and a slower large-angle 2-site jump mode with the angle between the orientations of 90°. An additional example yielding similar qualitative conclusions is shown in Figure S3, with the motional model and its parameters similar to the case of FMOC-methionine-D_3.

Thus, in general the observed experimental relaxation rate is expected to be different for the initial condition of the inversion along the tilted axis. As can be seen from Fig. 4, the overall amplitude change of the relaxation signal is significantly larger in the case of inversion, especially for large values of the offset Ω, and, therefore, experiments performed under the initial condition of inversion provide a more precise measurements of relaxation rates, in analogy to the accuracy of the inversion recovery experiment for the laboratory frame relaxation rate measurements.

3.3. FMOC-methionine amino acid

I. Description of the FMOC-methionine structure and the motional model for large angle jumps

FMOC-methionine (Fig. 1A) has a long methyl bearing side chain and the FMOC group that mimics hydrophobic environments, such as those found in proteins' hydrophobic cores [37,47,48]. As such, it is a interesting model system for NMR technique development with application to studies of molecular motions. The long side chain of methionine has three dihedral angles, which, in principle, permit for 27 rotameric states. Of course, not all of these states are populated in restricted environments, and, as such, we have found that the approximation of four symmetrical conformers with tetrahedral geometry is a sufficient model of rotameric inter-conversions in methionine [37]. In addition to the rotameric inter- conversion, there are fast methyl three-site jumps that average the effective value of the quadrupolar coupling constant to 58.3 kHz [25,42].

II. Implementation of the $R_{1\rho}^{off}$ measurements

We will use FMOC-methionine to demonstrate the applicability of the $R_{1\rho}^{off}$ experiment with and without the optional inversion pulse (Fig. 2) under static and 10 kHz MAS conditions, the use of the *tanh*/tan ramp alignment, and a joint fit of the line shape and $R_{1\rho}^{off}$ data.

The experimental static powder pattern is narrowed compared to what is expected in the absence of large angle motions (Fig. 5), with the abrupt drop of intensity at around ± 14.4 kHz. With this narrowing, we expect a relatively efficient locking with greater than $24\omega_{RF}$–30 kHz, based on prior detailed analysis of the spin-locking behavior in dimethyl-sulfone [15,24]. When performing experiments under MAS, an additional consideration is to choose the ω_{RF} value away from the major rotary resonance conditions, given by $\omega_{eff} = \frac{n}{2}\omega_{MAS}$, as discussed in the "Experimental approach" section. We thus choose ω_{MAS} = 10 kHz, andω_{RF} = 30 kHz. At the static condition we also perform measurements at ω_{RF} of 20 and 30 kHz. In the Supporting Information (Figure S4) we show one example of data obtained under 60 kHz MAS, indicating extensive presence of rotary resonances.

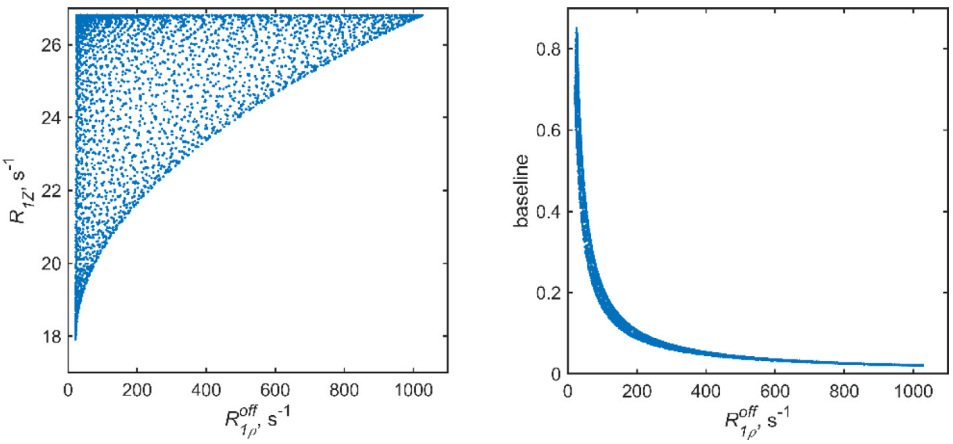

Fig. 4. A): A correlation plot of $R_{1\rho}^{off}$ with R_1 for individual crystallites. The rates are calculated according to Eqs. (13) and (15). B) The correlation of $R_{1\rho}^{off}$ with the relaxation baseline b for individual crystallites. The baseline values are obtained according to Eq. (13). The Larmor frequency was $\frac{\omega_L}{2\pi} = 61.4$MHz, $C_q = 165$kHz, $\frac{\omega_{RF}}{2\pi} = 30$kHz, and $\frac{\Omega}{2\pi} = 40$kHz. 6765 different crystallite orientations are included. The rate constant for three-site jumps was set to $5 \cdot 10^9 s^{-1}$, and the 90° 2-site jumps were modeled with rate constant of $5 \cdot 10^3 s^{-1}$.

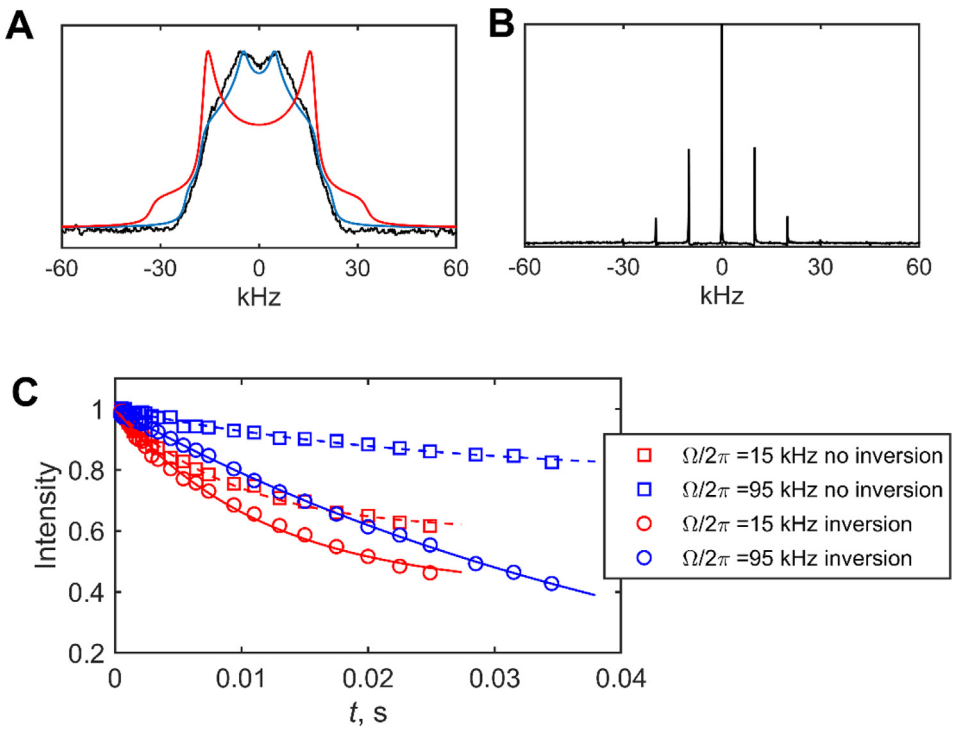

Fig. 5. $R_{1\rho}^{off}$ data for FMOC-Methionine-D_3 at static conditions, 9.4 T and 303 K, and at 10 kHz MAS conditions, 14.1 T and 310 K. A) A normalized experimental static QE spectrum (black) overlaid with the simulations according to the model of Fig. 1A with $k_{rot} = 2{\cdot}10^7$ s^{-1} and the ratio of rotameric populations of 13:1:1:1 (red) or $k_{rot} = 2{\cdot}10^7$ s^{-1} and the ratio of 13:6:1:1 (blue) with C_q = 58.3 kHz. The simulated line shapes employed additional line broadening of 2 kHz in comparison to the experimental spectrum. B) The spectrum at the 10 kHz MAS condition. C) Examples of magnetization decay curves for the $R_{1\rho}^{off}$ measurements at the static conditions and the spin-locking field of 30 kHz with and without the optional inversion pulse of Fig. 2. The two different values of the off-resonance offsets are shown directly on the panels. The integrated intensities were collected over the entire spectral region. The lines represent the fit to the monoexponential function with baseline of Eq.(1). The *tanh*/tan ramp of Eq. (2) was employed for magnetization alignment with α = 1.5, β = 5, and Ω_0 = 120 kHz. (For interpretation of the references to colour in this figure legend, the reader is referred to the web version of this article.)

The values of offsets are chosen to cover the tilt angles between about 9 to 80°. The adiabatic alignment was achieved with the *tanh*/tan ramp of Eq.(2) with a = 1.5, β = 5, and Ω_0 of 120 kHz. The efficiency of alignment against the theoretical values was tested for one case under static conditions: $\Omega/2\pi$=5kHz, ω_{RF}=30 kHz for Ω_0 values of 120 kHz and 80 kHz and coincided within the error bars with the calculations of Fig. 3A. Another experimental consideration is to minimize RF-induced heating to the sample, and for that reason we use the interscan delay of 1.8 s forω_{RF} = 20 kHz and 2.4 forω_{RF} = 30 kHz. These delays were previously optimized based on the T_1 times of deuterated dimethyl sulfone, whose relaxation times are very sensitive to slight changes in temperature [24]. The maximum relaxation time during the spin-lock period was set to 35 ms, again as the pre-caution to minimize RF-induced heating. The heat-compensation block of Fig. 2 ensured that the total RF-induced heating was the same for all relaxation delays. The heat compensation pulse has a square shape, to provide the same constant amplitude time period for different relaxation delays. For the static case, the detection block of Fig. 2 was modified to incorporate the QE scheme with the 30–35 μs echo time, which minimizes phase distortions due to probe ringing effects [18].

The magnetization decay curves (Fig. 5 and Figure S5) were sampled over the entire powder pattern in the static case and integrated over all sidebands in the MAS case. The data were fitted to the mono-exponential function with baseline (Eq. (1)) to account for infinite sampling time and a clear presence of the baseline in the experimental data. Forω_{RF} = 30 kHz two versions of the experiment were collected: with and without the optional inversion pulse. As expected, the numerical value of the baseline is strongly affected by the inversion pulse, especially for large values of offsets for which the T_1 contribution to the relaxation is significant. This effect is more pronounced when the T_1 value is large compared to the on-resonance rotating frame $T_{1\rho} = 1/R_{1\rho}$ relaxation time.

The T_1 contribution was measured independently by the inversion recovery measurements (Figure S6) and the resulting values were: 135 ± 5 ms for the 10 kHz MAS conditions and 114 ± 5 ms for the static conditions. The differences between static and MAS values reflect some differences in temperatures. The on-resonance relaxation time $T_{1\rho}$ is 10–11 ms, which is significantly smaller than the T_1 value, accentuating the need to include the limited sampling of the magnetization decay curves in calculations and fitting procedures. In general, the off-resonance $R_{1\rho}^{off}$ measurement will be more accurate for systems with smaller values of the ratio $T_1/T_{1\rho}$. In this sense the methionine side-chains with relatively long T_1 values at room temperatures, compared to those typically found leucine and valine residues [19,41,42], is a challenging test of the method.

As explained in the Theory section, the resulting $R_{1\rho}^{off}$ rates, displayed in Fig. 6, in the presence and absence of the inversion do not necessarily coincide. The reader is referred also to Eqs. (13)–(15). Further, larger experimental uncertainties are expected for the experiment in the absence of inversion, which is corroborated by the data. Once we discuss the model's parameters, we will also directly compare the experimental ratio of $R_{1\rho}^{off}$ values with and without the inversion against the calculations.

One additional confirmation of the validity of the experiment is to assess any potential differences in the positive and negative values of off-resonance offsets. In cases where the isotropic chemical

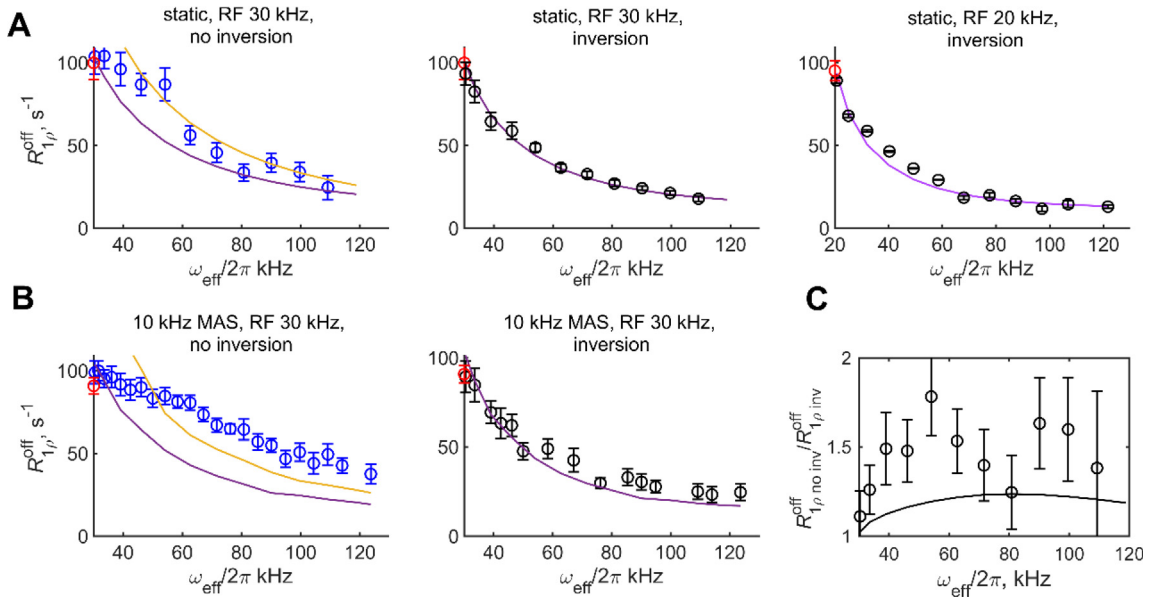

Fig. 6. $R_{1\rho}^{off}$ rates in FMOC-Methionine-D_3 versus ω_{eff} at A) static conditions, 9.4 T and 303 K, and B) 10 kHz MAS conditions, 14.1 T and 310 K with (black circles) or without (blue circles) the inversion pulse of Fig. 2. The values of ω_{RF} are indicated directly on the panels. The red circles represent the values of the on-resonance $R_{1\rho}$ relaxation rates. The lines represent the best fit according to the model of Fig. 1A with the rotameric weights in the 13:6:1:1 ratio and k_{rot} of either $2{\cdot}10^7$ s^{-1} (yellow line) or $k_{rot} = 4{\cdot}10^7$ s^{-1} (purple line), and $C_q = 58.3$ kHz. C) Experimental (black circles) and simulated (line) ratio of $R_{1\rho}^{off}$ rates with and without the inversion pulse. The simulations were performed with $k_{rot} = 4{\cdot}10^7$ s^{-1}. (For interpretation of the references to colour in this figure legend, the reader is referred to the web version of this article.)

shift interaction is the major contributor to the $R_{1\rho}^{off}$ rates (such as the case for ^{13}C and ^{15}N-based $R_{1\rho}^{off}$ measurements) [2,49], and the chemical shift of the conformers is significantly different, the relaxation rates can differ for positive and negative values of the offsets. In our case the symmetry of the quadrupolar interaction, which is the major contributor to the ^{2}H $R_{1\rho}^{off}$ relaxation, is such that no difference should be observed if the alignment is performed correctly: for negative offsets the adiabatic sweep should start with $-\Omega_0$. The equivalence of results from negative and positive offset values was confirmed experimentally. We have also tested one additional mode of alignment in which the adiabatic pulse is designed in such a way that the effective field is constant throughout the pulse. The results are presented in Figure S7 and yield identical $R_{1\rho}^{off}$ dispersion profiles to that of the more conventional alignment of Eq. (2).

Due to the presence of multiple protons in this model compound as well as in selectively deuterated peptides that we employ, we have performed a version of the measurements in the presence of proton decoupling during the spin-lock times for the 10 kHz MAS condition to test for potential coherent contributions from proton dipolar network. We have not observed any changes in the resulting magnetization decay curves. This indicates that simulations of the relaxation rates need to take into account only the quadrupolar interaction terms.

III. Fitting $R_{1\rho}^{off}$ rates and line shape data to the motional model

Our next goal is to define the motional model and the corresponding parameters that can explain both the line shapes and the $R_{1\rho}^{off}$ data (Figs. 5 and 6). In order to parametrize the rotameric mode of Fig. 1A with four symmetrical conformers, we need to know the relative weights (w_1:w_2:w_3:w_4) and the rotameric interconversion rate constant k_{rot}, defined as the sum of the forward and backward rates. In addition to these large angle fluctuations there are also fast methyl three-site jumps, which may or may not have an influence on the $R_{1\rho}$ rates beyond in three-fold decrease in the value of C_q. Another possible motional mode are smaller-angle fluctuations within the rotameric wells [19,42,47]. These fluctuations usually lead to subtler modifications of line shapes compared to the large-angle jumps, such as further narrowing of the distance between the "horns" of the powder pattern and slanting of the "shoulders" of the powder pattern. If they occur on a very fast time scale, they may not have an effect on the $R_{1\rho}$ values in the presence of the more effective slower large-angle jumps mode.

Our fitting strategy is to first obtain a rough match of the model parameters for the values of the on resonance $R_{1\rho}$ rate and the shape of the QE pattern, focusing on the rotameric interconversion mode. We start with the simplest assumption of a single major conformer and three equivalently populated minor conformers in w:1:1:1 ratio and a single rotameric rate. With this assumption, in order to approximately match the on-resonance $R_{1\rho}$ rate of 100 s^{-1} at 30 kHz spin-lock field strength, one needs the k_{rot} value on the order of 1.5 to 4.5 $\cdot 10^7$ s^{-1} with the value of w in the range of 2–20. As usual, there is a correlation in the fitted values of w and k_{rot} when only a single temperature is considered [50]. However, the simulated line shape under these ranges of parameters (see Fig. 5A red line, shown for $w = 13$) is very far off from the experimental one. The next step is to assign unequal weights to two out of the four conformers in the w_1:$w2$:1:1 ratio. This approach has also been used for joint fitting of the line shape and ^{2}H quadrupolar CEST data of Met-35 side chain of Aβ fibrils [20,38]. The line shapes are significantly more sensitive to the numerical values of the weights (Figure S8) in comparison to the on and off resonance $R_{1\rho}$ rates (Figure S9). If we keep the k_{rot} value in the range necessary to approximately fit the on resonance $R_{1\rho}$ value of 100 s^{-1}, which is given by k_{rot} of 2-4$\cdot 10^7$ s^{-1}, then the required ratio of populations is 13:6:1:1. Several examples of simulated line shapes are shown in Figure S8 to demonstrate the sensitivity of the fits to the values of w_1 and w_2.

The experimental line shape has a clear slanting of the shoulders, as well as the narrowed widths between the barely visible horns of the powder pattern. Mechanistically, this indicates the presence of smaller-angle motions inside the rotameric wells. Intra-well motions much faster than inter-well jumps have a

negligible effect on the $R_{1\rho}$ rates. Its effect on the line shape can be very roughly included as additional exponential line broadening. Thus, all simulated static spectra for FMOC methionine are shown with an extra line broadening of 2 kHz in comparison to the experimental data. Deuteron-deuteron dipolar interaction and potential contributions from proton dipolar network could also be partially responsible this broadening [51] and we are not able to distinguish the two effects based on the line shape alone. The presence of intra-well motions was shown in our prior work based on the temperature dependence of T_1 longitudinal relaxation times in FMOC-methionine in a wide temperature range of 325–150 K [48]. On the other hand, the fact that the proton decoupling does not change the observed rotating frame relaxation rate at a low MAS of 10 kHz indicates that the residual inhomogenous broadening due to proton dipolar network is relatively minor. A more quantitative approach of the effect of the intra-well motions on the line shapes is explored in the Leu-387 H6 peptide section. We emphasize that while in our approach the effects of motions are included in explicit motional modeling, it is possible to draw comparison to effective tensor characterization obtained using modern site-specific approaches [25–29] by calculating the resulting values of effective quadrupolar coupling constants and asymmetries, or even order parameters.

We do not need to include the additional fast methyl jumps mode into simulations of $R_{1\rho}^{off}$ rates, because the rotameric mode alone yields T_1 value of 97–183 ms. The three-site fast methyl jumps with the rate constant greater than $1\cdot 10^{10}$ s^{-1} are not an effective mechanism of T_1 relaxation in the presence of the rotameric motions, which are closer to the Larmor frequency.

Finally, once the range of parameters is narrowed, we perform simulations with the relative weights of 13:6:1:1 and a range of k_{rot} values around $1\text{-}5\cdot 10^7$ s^{-1} for the entire relaxation dispersion profiles obtained with and without the inversion pulse. The best fit for both static and 10 kHz MAS condition (shown in the solid lines Fig. 6) in the presence of the inversion pulse is given by the $k_{rot} = 4\cdot 10^7$ s^{-1}. An example of the fit's sensitivity to the rate constant values is shown in Figure S10. The fit in the absence of the inversion pulse (collected at 30 kHz spin-lock field only) is not as good, with the pattern of simulations deviating from the experimental line. As the precision for the non-inversion experiment is worse, it is more prone to experimental imperfections, such as RF inhomogeneity, which may obscure some features of the dispersion profile.

We also compare the experimental ratio of the $R_{1\rho}^{off}$ rates with and without the inversion pulse to the calculated ratio using the best-fit model parameters. While there is a qualitative agreement, the shape of the experimental profile is again somewhat different from the computed one, due to the discrepancies in the dispersion profile of the data without the inversion pulse (Fig. 6C). Unlike the theoretical calculations of Fig. 4 and Figure S3 (the latter one with the model parameters matching what we have found for the FMOC-methionine system), the computations in this case involved the full Liouvilian approach.

Another good control for the validity of the model is to perform complementary ^{2}H CEST measurements, which should be sensitive to the same types of motions and are expected to be consistent with the same model and its parametrization. We have performed such measurement at the 60 kHz MAS condition, presented in Figure S11, which cross-validated the results obtained from the $R_{1\rho}^{off}$ experiment.

3.4. N-terminal disordered domain of $A\beta_{1\text{-}40}$ fibrils

$A\beta_{1\text{-}40}$ fibrils, which comprise deposit in brains of patients with Alzheimer's disease, form a complex biomolecular system for which multiple structural and dynamic investigations have been performed [33,52–55]. The structure of the fibrils consists of the hydrophobic core spanned by β-sheets and a disordered N-terminal domain [33,34,52,53]. We have extensively studied the dynamics of the disordered domain with ^{2}H solid-state NMR and determined that it undergoes a conformational exchange between at least two states: a free state that undergoes large scale rearrangements and leads to significant spectral narrowing (Fig. 7A) and a bound state, in which the domain transiently interacts with the core and the large scale rearrangements are quenched [15,31,32,56]. The labeled methyl group of A2-CD_3 is located at the N-terminal flexible terminus.

We applied the $R_{1\rho}^{off}$ experiments to the hydrated $A\beta_{1\text{-}40}$ fibrils in its 3-fold symmetric polymorph [33,34] using the spin-locking field of 15 kHz strength under static conditions. The lower spin-locking amplitude is sufficient in this case because of the significantly smaller value of the effective tensor in the free state (the value of C_q is in around 3 kHz) [31] and helps in controlling the RF-induced heating, which would be detrimental to the sample. The adiabatic alignment can be achieved using the *tanh*/tan shape

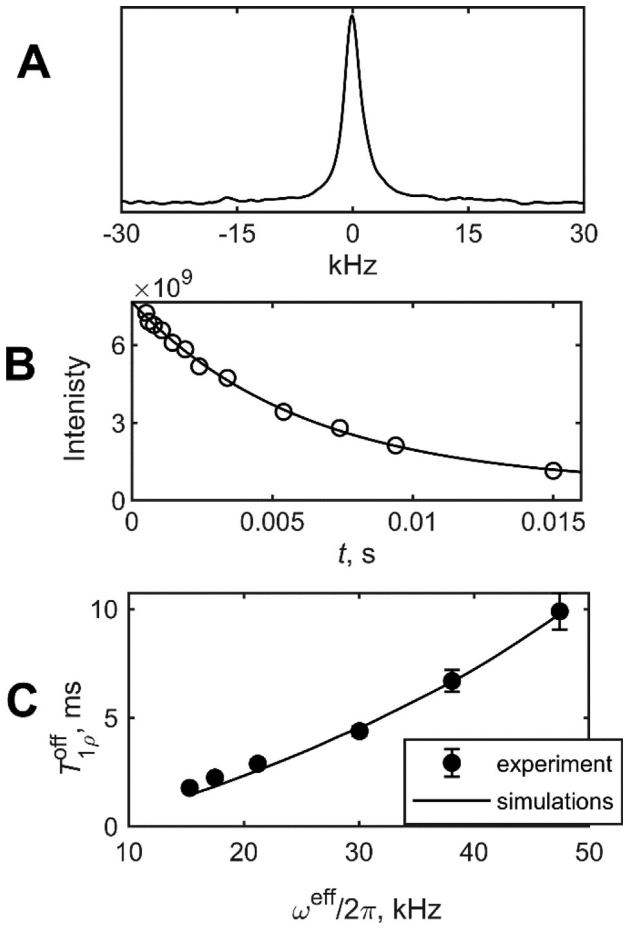

Fig. 7. Experimental data for A2-CD_3 methyl site in the disordered N-terminal domain of $A\beta_{1\text{-}40}$ fibrils, obtained at 14.1 T and 310 K under static conditions. A) Experimental ^{2}H line shapes using the QE pulse sequence.[31] B) An example of $R_{1\rho}^{off}$ magnetization decay curve for the spin-locking field of 15 kHz, the offset value of 35 kHz and other parameters detailed below. The intensities were integrated over the − 2.5 to 2.5 kHz spectral region. The line shows the fit to the monoexponential function with baseline of Eq. (1). C) The relaxation times, $T_{1\rho}^{off} = 1/R_{1\rho}^{off}$, (black circles) versus ω_{eff}. The tanh/tan ramp of Eq. (2) was employed for magnetization alignment with α = 1.5, β = 5, $\Omega_{0=}$ 40 kHz, and the spin-locking field of 15 kHz. The line represents the simulations according to the model of Fig. 1B with $D = 3.5\cdot 10^6$ rad^2/s and $k_{ex} = 3\cdot 10^4$ s^{-1}, and $p_{bound} = 0.08$.

with the 40 kHz sweep-width. The longitudinal relaxation time is measured to be 35 ms (Figure S6).

The results are shown in Fig. 7. We apply the previously developed model of Fig. 1B [31], which consists of several fitting parameters: the fraction of the bound state which was determined from the line shape decomposition as 0.08. The conformational exchange constant k_{ex} and the effective isotropic diffusion coefficient D, representing the large-scale rearrangements of the free state. The R_1 factor was taken into account phenomenologically, by including an additional term in the Liouvillian evolution matrix, which was identical for all eight coherences of Eq. (3) [38]. The parameters obtained from the prior on-resonance ^{2}H $R_{1\rho}$ results at static conditions were $D = 3.5{\cdot}10^6$ rad^2/s and $k_{ex} = 3\cdot10^4$ s^{-1} with $p_{bound} = 0.08$. This same set or parameters yields a good fit to the new $R_{1\rho}^{off}$ data. Thus, in this case we have confirmed the model, but we did not obtain any further insights in comparison to the on-resonance experiments [15].

3.5. H6 helix measurements permit for model refinement

The H6 helix is a 15-residue peptide which was labeled at a single residue of Leu-387. The synthesis leads to 50% labeling for each of the two prochiral methyl groups of the leucine. The numbering of the residue corresponds to its position in the full length α-helical domain construct of apoB protein (Fig. 1C). The peptide, produced by the solid-state peptide synthesis, was solvated with triolein to 50% weight content. Thus, if there are any differences between the two methyl groups, our results will be an average of the two sites.

Our goal is to determine the rotameric inter-conversion dynamics for the leucine residue in this peptide. The static QE line shape indicates two essential features in comparison to the rigid-like pattern that would be expected in the absence of slow motions but in the presence of fast methyl three-site jumps, shown in Figure S12A. One observes the rise of the intensity in the central component, which is due to the large-angle motions of the side chain as a result of rotameric interconversions, as well as an additional narrowing of the distance between the "horns" which arises due to smaller-angle restricted motions within the rotameric wells. It is sufficient in this case to model the rotameric interconversion with the two-site model of the effective 109.5° angle jumps, representing the exchange between the two most likely conformers of the leucine side chain: $\chi_1 = 300°$ $\chi_2 = 180°$ and $\chi_1 = 180°$ $\chi_2 = 60°$. (Fig. 1C) [57]. Theoretically there are nine conformers in the leucine side-chain, whose weights depend heavily on the surroundings. The two-site exchange model suggests a relatively restricted environment allowing for significant populations of only two conformers. Their relative weights do not have to be equal. The small-angle fluctuations within the rotameric wells can be fitted within a variety of models, out of which the model of the restricted arc motions of the methyl axis has proven to be a good choice in leucine side-chains of different protein systems [19,50]. The line shape can be fitted well with the rotameric exchange rate constant k_{rot} of 2000 s^{-1} and the additional mode of fast restricted arc motions with the arc length of 45° and the rate constant in the fast limit with respect to the value of C_q. We have assumed the population of rotameric states in the 2:1 ratio, which is reasonable assumption given an asymmetric environment around the side chain. This ratio cannot be determined unambiguously from the data at a single temperature, as there is a significant correlation between the value of k_{rot} and the relative weights of the rotamers. The central very narrow peak in the spectrum represents residual natural abundance ^{2}H signal from triolein solvent and is not included in the simulations.

The $R_{1\rho}^{off}$ experiments in this case were performed under MAS conditions with 10 kHz spinning rate, with employment of the *tanh*/tan ramp using the value of sweep width of 120 kHz. Two values of spin-locking field of 17 and 30 kHz were used. The spectrum

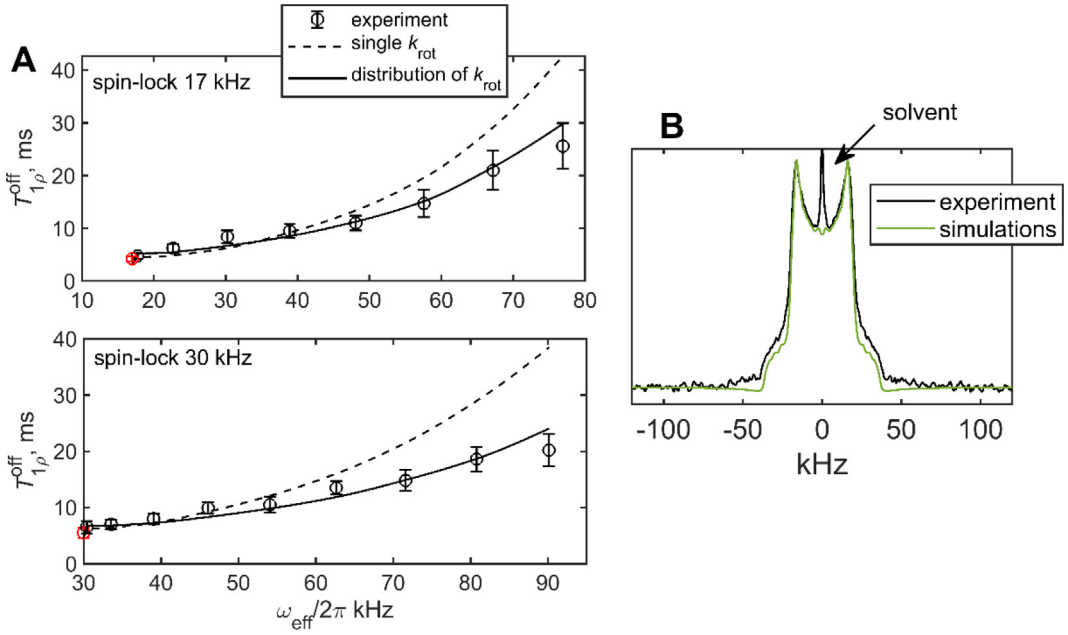

Fig. 8. Experimental data for the H6 helical peptide hydrated with triolein and with the deuterium label on the Leu-387 methyl group. A) Relaxation times, $T_{1\rho}^{off}$, (black circles) versus ω_{eff} for two values of spin lock fields indicated on the panels. The red circles represent the on-resonance relaxation time. The data were collected at 14.1 T and 295 K with the 10 kHz MAS rate. The dotted line shows the fit to the two-site rotameric exchange model of Fig. 1C with a single k_{rot} values of 2000 s^{-1} and populations of the states in the 2:1 ratio. The solid line represents the fit to the model involving a distribution of rotameric rates around this central value, as detailed in the text. B) The experimental ^{2}H line shape under static conditions collected at 9.4 T and 295 K with the quadrupolar echo detection scheme (black) overlayed with simulations according to the two-site rotameric exchange model with the single value of $k_{rot} = 2000$ s^{-1}. An additional mode of fast fluctuations within the rotameric well is included, as described in the text. The central peak represents residual natural abundance triolein signal. (For interpretation of the references to colour in this figure legend, the reader is referred to the web version of this article.)

under MAS conditions and examples of magnetization decay curves are shown in Figure S13, in which the sum of all sidebands' intensities have been used. The ^{2}H T_1 relaxation time, dominated by fast methyl three-site jumps, was measured to be 51 ms (Figure S6). Note, that the single-exponential nature of the two magnetization decay curves suggests no major differences between the two leucine methyl sites within the precision of these measurements.

When the $R_{1\rho}^{off}$ rates are simulated according to the 2-site exchange model with a single rotameric rate of k_{rot} = 2000 s^{-1} and the 2:1 population ratio, there is a discrepancy in the experimental and simulated trend, with the extent of deviations increasing for larger values of offsets (Fig. 8A, dashed line). The fast motions within the rotameric well have a negligible effect on the relaxation rate (under 2–3% for our ranges). The R_1 factor was included phenomenologically into the $R_{1\rho}^{off}$ simulations [38], as explained in the previous sections.

Thus, we need a modified model to describe the ^{2}H $R_{1\rho}^{off}$ data. One of the possibilities is to include a distribution of rotameric rates, while maintaining the central value of 2000 s^{-1}. To achieve an agreement with the experiment we have used a uniform distribution over ln k_{rot}, the width of which is 1.6 (Fig. 8A, solid line). As was the case for the line shapes, there is also the ambiguity/correlation between the choice of the relative weights of the rotamers and the value of k_{rot} (Figure S14 and S15), shown for the on-resonance $R_{1\rho}$). As a control for this more complex model, we have confirmed that the fitted line shapes in the presence of the distribution of k_{rot} are very similar to the single rate fit (Figure S12B). The need for this distribution signifies a more complex heterogenous environment around the methyl groups, which might be responsible for binding properties of the H6 helix.

Additionally, we have explored the idea of enhancing the deuterium polarization via proton-deuterium Hartmann-Hahn cross-polarization (CP) prior to the deuterium rotating frame relaxation period. This polarization step, in principle, can also be useful for studies involving indirect dynamic nuclear polarization [58]. The H6 construct is a good candidate to evaluate the efficiency of the enhancement in biological systems due to low proton T_1 relaxation time of 0.8 s, as well as due to relative proximity of directly bonded protons to the deuterated methyl group in the leucine side-chain. With the ramped-CP approach [59] the best efficiency of the enhancement did not exceed 1.25. The optimized CP contact time of 3 ms and the RF fields of 42 kHz on ^{2}H and 52 kHz on ^{1}H were employed. A linear amplitude ramp between 70 and 100% was used on deuterium during the contact time. The relatively low efficiency is likely due to the mobility of the methyl -bearing side chain and the C_q value of 55 kHz for the quadrupolar interaction.

In conclusion, we have demonstrated the ^{2}H $R_{1\rho}^{off}$ measurements could be a useful tool for investigations of molecular dynamics in a variety of biomolecular systems. We note that special care has to be taken for the optimization of the alignment of magnetization along the tilted axis and the choice of RF field amplitude for the spin-lock under MAS conditions to achieve sufficient locking without encountering potential complications caused by rotary resonances. The values of the $T_1/T_{1\rho}$ ratio can somewhat affect the sensitivity of the measurements to slow motions and guide the choice of the relaxation delays employed in the measurements.

We have demonstrated that these techniques can be applied to amyloid fibrils and large triacylglycerol emulsions, systems that are notoriously difficult to access. The methods described here provide new means to investigate details of internal motions in large and complex systems.

Data availability

Data will be made available on request.

Declaration of Competing Interest

The authors declare that they have no known competing financial interests or personal relationships that could have appeared to influence the work reported in this paper.

Acknowledgements

This work was supported by a National Institutes of Health Grant 1R15-GM111681 and NSF-MRI instrumentation grant CHE-1726947. Part of the measurements were performed at the National High Magnetic Field Laboratory, which is supported by NSF Cooperative Agreement NSF/DMR-1644779 and DMR-2128556, the State of Florida, and the U.S. Department of Energy.

Appendix A. Supplementary material

Supplementary data to this article can be found online at https://doi.org/10.1016/j.jmr.2023.107493.

References

[1] D.D. Boehr, R. Nussinov, P.E. Wright, The role of dynamic conformational ensembles in biomolecular recognition, Nat. Chem. Biol. 5 (2009) 789–796.
[2] P. Schanda, M. Ernst, Studying dynamics by magic-angle spinning solid-state NMR spectroscopy: Principles and applications to biomolecules, Prog. Nucl. Magn. Reson. Spectrosc. 96 (2016) 1–46.
[3] A.G. Palmer 3rd, Chemical exchange in biomacromolecules: past, present, and future, J. Magn. Reson. 241 (2014) 3–17.
[4] N.-A. Lakomek, S. Penzel, A. Lends, R. Cadalbert, M. Ernst, B. Meier, Microsecond dynamics in ubiquitin probed by solid-state NMR 15N R1rho relaxation experiments under fast MAS (60–110 kHz), Chemistry 23 (2017) 9425–9433.
[5] A. Krushelnitsky, T. Zinkevich, B. Reif, K. Saalwächter, Slow motions in microcrystalline proteins as observed by MAS-dependent 15N rotating-frame NMR relaxation, J. Magn. Reson. 248 (2014) 8–12.
[6] V. Kurauskas, S.A. Izmailov, O.N. Rogacheva, A. Hessel, I. Ayala, J. Woodhouse, A. Shilova, Y. Xue, T. Yuwen, N. Coquelle, J.-P. Colletier, N.R. Skrynnikov, P. Schanda, Slow conformational exchange and overall rocking motion in ubiquitin protein crystals, Nature Commun. 8 (2017) 145.
[7] C. Quinn, A. McDermott, Monitoring conformational dynamics with solid-state R1r experiments, J. Biomol. NMR 45 (2009) 5–8.
[8] P. Ma, J.D. Haller, J. Zajakala, P. Macek, A.C. Sivertsen, D. Willbold, J. Boisbouvier, P. Schanda, Probing transient conformational states of proteins by solid-state R(1ρ) relaxation-dispersion NMR spectroscopy, Angewandte Chem. (Int Ed.) 53 (2014) 4312–4317.
[9] D.F. Gauto, A. Hessel, P. Rovó, V. Kurauskas, R. Linser, P. Schanda, Protein conformational dynamics studied by 15N and 1H R1ρ relaxation dispersion: Application to wild-type and G53A ubiquitin crystals, Solid State Nucl. Magn. Reson. 87 (2017) 86–95.
[10] P. Rovó, R. Linser, Microsecond timescale protein fynamics: a combined solid-state NMR approach, ChemPhysChem 19 (2018) 34–39.
[11] P. Rovó, R. Linser, Microsecond time scale proton rotating-frame relaxation under magic angle apinning, J. Phys. Chem. B 121 (2017) 6117–6130.
[12] D. Marion, D.F. Gauto, I. Ayala, K. Giandoreggio-Barranco, P. Schanda, Microsecond protein dynamics from combined Bloch-McConnell and near-rotary-resonance R(1p) relaxation-dispersion MAS NMR, Chemphyschem 20 (2019) 276–284.
[13] A. Krushelnitsky, D. Gauto, D.C. Rodriguez Camargo, P. Schanda, K. Saalwachter, Microsecond motions probed by near-rotary-resonance R1rho (15)N MAS NMR experiments: the model case of protein overall-rocking in crystals, J. Biomol. NMR 71 (2018) 53–67.
[14] P. Rovó, Recent advances in solid-state relaxation dispersion techniques, Solid State Nucl. Magn. Reson. 101665 (2020).
[15] L. Vugmeyster, D. Ostrovsky, A. Greenwood, R. Fu, Deuteron rotating frame relaxation for the detection of slow motions in rotating solids, J. Magn. Reson. 337 (2022).
[16] P. Schanda, Relaxing with liquids and solids - A perspective on biomolecular dynamics, J. Magn. Reson. 306 (2019) 180–186.
[17] P. Rovó, C.A. Smith, D. Gauto, B.L. de Groot, P. Schanda, R. Linser, Mechanistic insights into microsecond time-scale motion of solid proteins using complementary 15N and 1H relaxation dispersion techniques, J. Am. Chem. Soc. 141 (2019) 858–869.

[18] R.L. Vold, R.R. Vold, Deuterium relaxation in molecular solids, in: W. Warren (Ed.), Advances in Magnetic and Optical Resonance, Academic Press, San Diego, 1991, pp. 85–171.
[19] L. Vugmeyster, D. Ostrovsky, Static solid-state 2H NMR methods in studies of protein side-chain dynamics, Prog. Nucl. Magn. Reson. Spec. 101 (2017) 1–17.
[20] L. Vugmeyster, Recent developments in deuterium solid-state NMR for the detection of slow motions in proteins, Solid State Nucl. Magn. Reson. 111 (2021).
[21] A.V. Struts, G.F.J. Salgado, K. Martnez-Mayorga, M.F. Brown, Retinal dynamics underlie its switch from inverse agonist to agonist during rhodopsin activation, Natur. Struct, Mol. Biol. 18 (2011) 392–394.
[22] C. Sun, O. Mitchell, J.X. Huang, G.S. Boutis, NMR studies of localized water and protein backbone dynamics in mechanically strained elastin, J. Phys. Chem. B 115 (2011) 13935–13942.
[23] M.F. Brown, M.P. Heyn, C. Job, S. Kim, S. Moltke, K. Nakanishi, A.A. Nevzorov, A. V. Struts, G.F.J. Salgado, I. Wallat, Solid-state H-2 NMR spectroscopy of retinal proteins in aligned membranes, Biochim. Biophys. Acta, Biomembr. (2007, 1768,) 2979–3000.
[24] L. Vugmeyster, D. Ostrovsky, Deuterium rotating frame NMR relaxation measurements in the solid state under static conditions for quantification of dynamics, Chemphyschem 20 (2019) 333–342.
[25] X. Shi, C.M. Rienstra, Site-Specific Internal motions in GB1 protein microcrystals revealed by 3D 2H–13C–13C solid-state NMR Spectroscopy, J. Am. Chem. Soc. 138 (2016) 4105–4119.
[26] U. Akbey, A.J. Nieuwkoop, S. Wegner, A. Voreck, B. Kunert, P. Bandara, F. Engelke, N.C. Nielsen, H. Oschkinat, Quadruple-resonance magic-angle spinning NMR spectroscopy of deuterated solid proteins, Angew. Chem. 53 (2014) 2438–2442.
[27] Ü. Akbey, Dynamics of uniformly labelled solid proteins between 100 and 300 K: A 2D (2)H-(13)C MAS NMR approach, J. Magn. Reson. 327 (2021).
[28] Ü. Akbey, Site-specific protein backbone deuterium (2)H(α) quadrupolar patterns by proton-detected quadruple-resonance 3D (2)H(α)c(α)NH MAS NMR spectroscopy, Solid State Nucl. Magn. Reson. 125 (2023).
[29] M.D. Gelenter, K.J. Chen, M. Hong, Off-resonance (13)C-(2)H REDOR NMR for site-resolved studies of molecular motion, J. Biomol. NMR 75 (2021) 335–345.
[30] F.A.A. Mulder, R.A. de Graaf, R. Kaptein, R. Boelens, An Off-resonance rotating frame relaxation experiment for the investigation of macromolecular dynamics using adiabatic rotations, J. Magn. Reson. 131 (1998) 351–357.
[31] D.F. Au, D. Ostrovsky, R. Fu, L. Vugmeyster, Solid-state NMR reveals a comprehensive view of the dynamics of the flexible, disordered N-terminal domain of amyloid-β fibrils, J. Biol. Chem. 294 (2019) 5840–5853.
[32] L. Vugmeyster, D.F. Au, D. Ostrovsky, R. Fu, Deuteron solid-state NMR relaxation measurements reveal two distinct onformational exchange processes in the disordered N-terminal domain of amyloid-b fibrils, ChemPhysChem 20 (2019) 1680.
[33] A.T. Petkova, R.D. Leapman, Z.H. Guo, W.M. Yau, M.P. Mattson, R. Tycko, Self-propagating, molecular-level polymorphism in Alzheimer's beta-amyloid fibrils, Science 307 (2005) 262–265.
[34] A.K. Paravastu, R.D. Leapman, W.M. Yau, R. Tycko, Molecular structural basis for polymorphism in Alzheimer's beta-amyloid fibrils, Proc. Natl. Aca. Sci. U.S. A. 105 (2008) 18349–18354.
[35] R.W. Mahley, T.L. Innerarity, S.C. Rall Jr., K.H. Weisgraber, Plasma lipoproteins: apolipoprotein structure and function, J Lipid Res 25 (1984) 1277–1294.
[36] M.A. Mitsche, L.E. Packer, J.W. Brown, Z.G. Jiang, D.M. Small, C.J. McKnight, Surface tensiometry of apolipoprotein B domains at lipid interfaces suggests a new model for the initial steps in triglyceride-rich lipoprotein assembly, J. Biol. Chem. 289 (2014) 9000–9012.
[37] L. Vugmeyster, M.A. Clark, B.I. Falconer, D. Ostrovsky, D. Gantz, W. Qiang, G.L. Hoatson, Flexibility and solvation of amyloid -beta hydrophobic core, J. Biol. Chem. 291 (2016) 18484–18495.
[38] L. Vugmeyster, D. Ostrovsky, R. Fu, Deuteron quadrupolar chemical exchange saturation transfer (Q-CEST) solid-state NMR for static powder samples: approach and applications to amyloid-β fibrils, ChemPhysChem 21 (2020) 220–231.
[39] L. Vugmeyster, D. Ostrovsky, J.J. Ford, S.D. Burton, A.S. Lipton, G.L. Hoatson, R.L. Vold, Probing the dynamics of a protein hydrophobic core by deuteron solid-state nuclear magnetic resonance spectroscopy, J. Am. Chem. Soc. 131 (2009) 13651–13658.
[40] P.-O. Persson, G. Strang, A Simple Mesh Generator in MATLAB, SIAM Rev. 46 (2004) 329–345.
[41] M.A. Keniry, A. Kintanar, R.L. Smith, H.S. Gutowsky, E. Oldfield, Nuclear magnetic-resonance studies of amino-acids and proteins - deuterium nuclear magnetic-resonance relaxation of deuteriomethyl-labeled amino-acids in crystals and in halobacterium-halobium and escherichia-coli cell-membranes, Biochemistry 23 (1984) 288–298.
[42] M.A. Keniry, T.M. Rothgeb, R.L. Smith, H.S. Gutowsky, E. Oldfield, uclear magnetic-resonance studies of amino-acids and proteins- side-chain mobility of methionine in the crystalline amino-acid and in crystalline sperm whale (Physeter-Catodon) myoglobin, Biochemistry 22 (1983) 1917–1926.
[43] A. Abragam, Principles of Nuclear Magnetism, Clarendon Press, Oxford, 1961.
[44] J.R.C. van der Maarel, The relaxation dynamics of spin 1=1 nuclei with a static quadrupolar coupling and a radio-frequency field, J. Chem. Phys. 99 (1993) 5646–5653.
[45] G.P. Jones, Spin-lattice relaxation in the rotating frame: weak-collision case, Phys. Rev. 148 (1966) 332–335.
[46] C.M. Quinn, A.E. McDermott, Quantifying conformational dynamics using solid-state R1ρ experiments, J. Biomol. NMR 222 (2012) 1–7.
[47] L. Vugmeyster, D. Ostrovsky, M. Moses, J.J. Ford, A.S. Lipton, G.L. Hoatson, R.L. Vold, Comparative dynamics of leucine methyl groups in FMOC-leucine and in a protein hydrophobic core probed by solid-state deuteron NMR over 7–324K temperature range, J. Phys. Chem. 114 (2010) 15799–15807.
[48] L. Vugmeyster, D. Ostrovsky, Comparative dynamics of methionine side-chain in FMOC-methionine and in amyloid fibrils, Chem. Phys. Lett. 673 (2017) 108–112.
[49] A.G. Palmer, NMR characterization of the dynamics of biomacromolecules, Chem. Rev. 104 (2004) 3623–3640.
[50] L. Vugmeyster, D. Ostrovsky, Basic experiments in 2H static NMR for the characterization of protein side-chain dynamics, Methods 148 (2018) 136–145.
[51] J. Hirschinger, H. Miura, K.H. Gardner, A.D. English, Segmental dynamics in the crystalline phase of NYLON-66 solid-state H-2 NMR, Macromol 23 (1990) 2153–2169.
[52] A.T. Petkova, W.M. Yau, R. Tycko, Experimental constraints on quaternary structure in Alzheimer's beta-amyloid fibrils, Biochemistry 45 (2006) 498–512.
[53] A.K. Paravastu, I. Qahwash, R.D. Leapman, S.C. Meredith, R. Tycko, Seeded growth of beta-amyloid fibrils from Alzheimer's brain-derived fibrils produces a distinct fibril structure, Proc. Natl. Aca. Sci. U.S.A. 106 (2009) 7443–7448.
[54] H.A. Scheidt, I. Morgado, S. Rothemund, D. Huster, Dynamics of amyloid beta fibrils revealed by solid-state NMR, J. Biol. Chem. 287 (2012) 2017–2021.
[55] E. Hubin, N.A.J. van Nuland, K. Broersen, K. Pauwels, Transient dynamics of A beta contribute to toxicity in Alzheimer's disease, Cell. Mol. Life Sci. 71 (2014) 3507–3521.
[56] L. Vugmeyster, D. Ostrovsky, A. Greenwood, R. Fu, Deuteron chemical exchange saturation transfer for the detection of slow motions in rotating solids, Front. Mol. Biosci. 8 (2021).
[57] L.S. Batchelder, C.E. Sullivan, L.W. Jelinski, D.A. Torchia, Characterization of leucine side-chain reorientation in collagen fibrils by solid-state H-2 NMR, Proc. Natl. Acad. Sci. U. S. A. 79 (1982) 386–389.
[58] A.S. Lilly Thankamony, J.J. Wittmann, M. Kaushik, B. Corzilius, Dynamic nuclear polarization for sensitivity enhancement in modern solid-state NMR, Prog. Nucl. Magn. Reson. 102–103 (2017) 120–195.
[59] G. Metz, X.L. Wu, S.O. Smith, Ramped-amplitude cross polarization in magic-angle-spinning NMR, J. Magn. Reson. A 110 (1994) 219–227.